Nano Research

Open Access

Research Article

Periodic nanopillar arrays integrated gold-capped silicon nanograsses with nanometer gap for large-area, uniform and sensitive surface-enhanced Raman scattering

Ni Zhang[1], Yi Liu[1], Xiaoyi She[1], Yang Shen[1], Xuelin Tian[2], and Chongjun Jin[1]✉

[1] *State Key Laboratory of Optoelectronic Materials and Technologies, Guangzhou Key Laboratory of Flexible Electronic Materials and Wearable Devices, School of Materials Science and Engineering, Sun Yat-sen University, Guangzhou 510275, China*
[2] *School of Materials Science and Engineering, Sun Yat-sen University, Guangzhou 510275, China*

Cite this article: *Nano Research*, **2026**, *19*, 94908563. https://doi.org/10.26599/NR.2026.94908563

ABSTRACT: Structured surface-enhanced Raman scattering (SERS) substrates that integrate plasmonic nanoparticles with tunable localized surface plasmon resonances are ideal for constructing gap nanostructures with hotspots. However, it remains challenging to create controllable nanogaps between plasmonic nanoparticles. In this work, we propose a hybrid nanostructure that integrates a two-dimensional periodic nanopillar array (PNA) with metal nanoparticle assemblies to regulate the spatial arrangement of hotspots and electromagnetic field coupling modes. Approximately 5-nm nanogaps were fabricated via reactive ion etching and subsequent Au deposition via magnetron sputtering. At the same time, the PNA periodicity was controlled by dual-beam interference lithography to match the laser excitation wavelength with the structure's optical resonance. The resulting high-density hotspots reduce molecular adsorption positional sensitivity, leading to enhanced reproducibility for rhodamine 6G with a relative standard deviation of 11.6%. Furthermore, the substrate achieves detection limits of 10, 1, and 100 nM for 4-nitrobenzenethiol, thiram and melamine molecules, respectively.

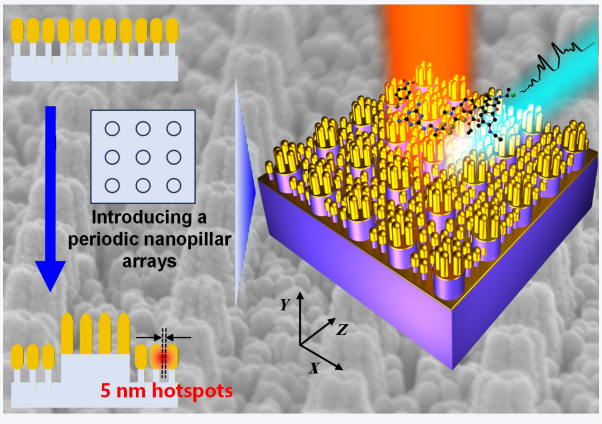

KEYWORDS: localized surface plasmon resonance, surface-enhanced Raman scattering, nanostructured arrays, hotspot intensity modulation, interference lithography

1 Introduction

Plasmonic nanostructure arrays serve as a powerful platform for light–matter interactions, enabling unique and rich optical properties with potential applications in surface-enhanced Raman scattering (SERS). SERS can amplify molecular fingerprint Raman signals by 6–10 orders of magnitude [1], facilitating ultra-sensitive trace detection or even single-molecule detection. It has rapidly developed into a robust trace analysis technique with broad application prospects in fields such as biomedical diagnosis [2, 3], environmental pollutant monitoring [4], and food safety detection [5, 6]. The enhancement mechanism of SERS primarily originates from the localized surface plasmon resonance (LSPR) effect, where the collective oscillation of free electrons on metal nanostructure surfaces significantly enhances the inelastic scattering cross-section of target molecules [7–9]. An ideal SERS substrate requires three key characteristics: strong localized electromagnetic fields to enhance signal intensity, high reproducibility to ensure detection reliability, and low-cost fabrication processes that enable practical applications. Current SERS substrate fabrication predominantly employs chemical synthesis and physical preparation methods. Chemical approaches facilitate the rapid synthesis of nanoparticles in solution, generating hotspots at particle tips and interparticle gaps that effectively enhance local electromagnetic fields. However, chemical methods are limited by the randomness of particle size and distribution, which leads to significant fluctuations in SERS signal intensity. In contrast,

Received: November 25, 2025; **Revised:** February 9, 2026
Accepted: February 12, 2026

✉Address correspondence to jinchjun@mail.sysu.edu.cn

physical methods (such as focused ion beam milling and electron beam lithography) enable precise control of plasmonic nanostructure morphology, thereby controlling hotspot intensity and distribution [10]. However, their high preparation cost, protracted fabrication duration, and insufficient hotspot density make them unsuitable for high-throughput trace detection applications. To address the limitations, previous studies have attempted to improve sensitivity and reproducibility through structural optimization. For instance, Shen et al. [11] proposed combining Au nanoparticles assembly with nanostructured photonic substrates to form a grating-integrated gold nanograss (GIGN) composite structure. These enhance the electric field via the coupling between surface plasmon polaritons (SPP) and LSPR, and the diffraction behavior of the structured substrate is utilized to regulate the spatial distribution of hotspots, demonstrating good reproducibility. Subsequently, this team further selectively coated the tips of the GIGN gold nanograss with a porous zeolitic imidazolate framework material (ZIF-8) [12], exhibiting a detection limit of 10^{-11} M for 4-aminothiophenol （4-ATP) with a relative standard deviation of 5.59% and a sigmoidal fitting curve (R^2 = 0.988) was achieved across a wide concentration range of 10^{-5}–10^{-11} M, demonstrating robust sensitivity and quantitative capability.

Sub-10 nm gaps in plasmonic nanostructures play a decisive role in SERS single enhancement. Gaps between adjacent nanostructures can form high-intensity hotspots, significantly boosting localized electromagnetic field strength. Although experiments have confirmed that substrates with tunable sub-20 nm gaps possess enhancement capabilities [13], theory indicates that optimized SERS performance requires gaps controlled at even lower nanoscales (1–10 nm), where plasmon resonance broadening and near-field coupling effects reach the peak [14]. When analytes reside in gaps smaller than 10 nm, the SERS single enhancement increases exponentially as the gap decreases [15]. Recently, researchers have explored large-scale fabrication methods such as colloidal nanoparticle self-assembly [15] and etching-assisted templating [13], in an attempt to achieve batch fabrication of sub-10 nm gaps by regulating the dynamic aggregation of nanoparticles. However, their poor reproducibility remains insufficient for commercial applications (commercial SERS substrates require a relative standard deviation below 20%) [16–18]. Therefore, nanogap arrays with small feature sizes, high density, and uniform distribution play a critical role in developing SERS substrates that exhibit high sensitivity and excellent signal reproducibility.

Here, we present a strategy combining controllable hotspot construction and large-scale fabrication. It involves introducing a two-dimensional (2D) periodic nanopillar array (PNA) into metal nanoparticle assemblies to regulate the spatial arrangement of hotspots and electromagnetic field coupling modes. ~ 5 nm average nanogaps were constructed by reactive ion etching (RIE) and subsequent Au deposition via magnetron sputtering. While the period of PNA was tuned to match the pumping laser wavelength with the structure's optical response, this allowed for the controllable construction of hotspot distribution and intensity. The high-density hotspots provided by the structured substrate reduce molecular positional sensitivity, leading to an enhanced SERS signal for rhodamine 6G (R6G) with a relative standard deviation (RSD) of 11.6%. The achieved detection limits for 4-nitrobenzenethiol (4-NBT), thiram and melamine molecules are 10, 1, and 100 nM, respectively.

2 Results and discussion

2.1 Design and preparation of PNA-Si@Au NG

A composite structure of periodic nanopillar arrays integrated with gold-capped silicon nanograsses (PNA-Si@Au NG) was developed, in which two-dimensional Si PNA were introduced into Si@Au nanograss assemblies, as shown in Fig. S1 in the Electronic Supplementary Material (ESM). The coupling between the in-plane diffraction excited by the PNA and the LSPR in the Si@Au nanograss aggregates enhances the localized electromagnetic field of the structure. The purposes of the introduction of PNA could be concluded as follows: Firstly, each Si nanopillar spatially isolates the underlying Si@Au nanograss assemblies from the upper layer ones, forming a bilayer-like 2D metal nanostructure array that induces inter-assembly coupling to enhance localized electromagnetic fields. Secondly, the resonant modes of this structure are primarily governed by the structural parameters of PNA, greatly reducing the impact of randomness in optical response caused by variations in geometric factors (e.g., size, shape, and interparticle gap distance) of metal nanoparticles. Figure 1(a) illustrates the schematic diagram of the PNA-Si@Au NG structure and its key structural parameters. The period, average diameter, and average height of the PNA are denoted as a, D, and H, respectively. It is worth noting that due to different Si etching rates at the bottom and top of the PNA, the average height of the Si@Au nanograsses varies, denoted as l_0 and l_1. d represents the average diameter of the Si@Au nanograsses. A continuous Au film, with thickness $t \approx 10$ nm, naturally forms during Au deposition. Furthermore, the gap between adjacent Si@Au nanograsses is controlled by RIE etching time and subsequent Au deposition via magnetron sputtering. The average gap in the x- and z-axes is denoted as s_x and s_z.

The fabrication of the PNA-Si@Au NG structure employed large-scale fabrication methods including dual-beam interference lithography, RIE, and magnetron sputtering. Figure 1(a) provides the fabrication process, primarily consisting of three steps: (1) preparation of the PNA photoresist arrays mask; (2) fabrication of periodic nanopillar arrays integrated silicon nanograss (PNA-Si NG); (3) deposition of PNA-Si NG by Au to form the PNA-Si@Au NG structure. First, a 2D periodic mushroom-like photoresist array (inset of Fig. 1(b)) was fabricated on a photoresist-coated Si substrate using two sequential exposures with the substrate rotation of 90° round the sample surface normal, as illustrated in Fig. 1(b). The structural periodicity was modulated by adjusting the angle between the incident direction of laser beams and the sample plane normal (Fig. S2 in the ESM). Subsequently, the exposed substrate was etched in an RIE system using an SF_6/O_2 gas mixture (the flow rates of SF_6 and O_2 were 13 and 10 sccm, respectively) at 8 mTorr chamber pressure and 50 W power for 1–6 min. After etching, residual organics were removed via an ultrasonic cleaning in acetone, yielding the PNA-Si NG nanostructure shown in Fig. 1(c). It is worth noting that Si nanograsses formed at both the base and top of the PNA. Although the top of PNA was initially protected by photoresist, Si nanograsses were formed by etching Si with SF_6 after the photoresist was consumed by O_2 within 40 s (Fig. S3 in the ESM). Finally, Au was deposited onto the PNA-Si NG structure surface via magnetron sputtering under the following conditions: Ar flow rate 45 sccm, current 35 mA, and deposition time 150 s, with the voltage ~ 360 V and chamber pressure ~ 1.7 Pa maintained during the process. The resulting PNA-Si@Au NG is

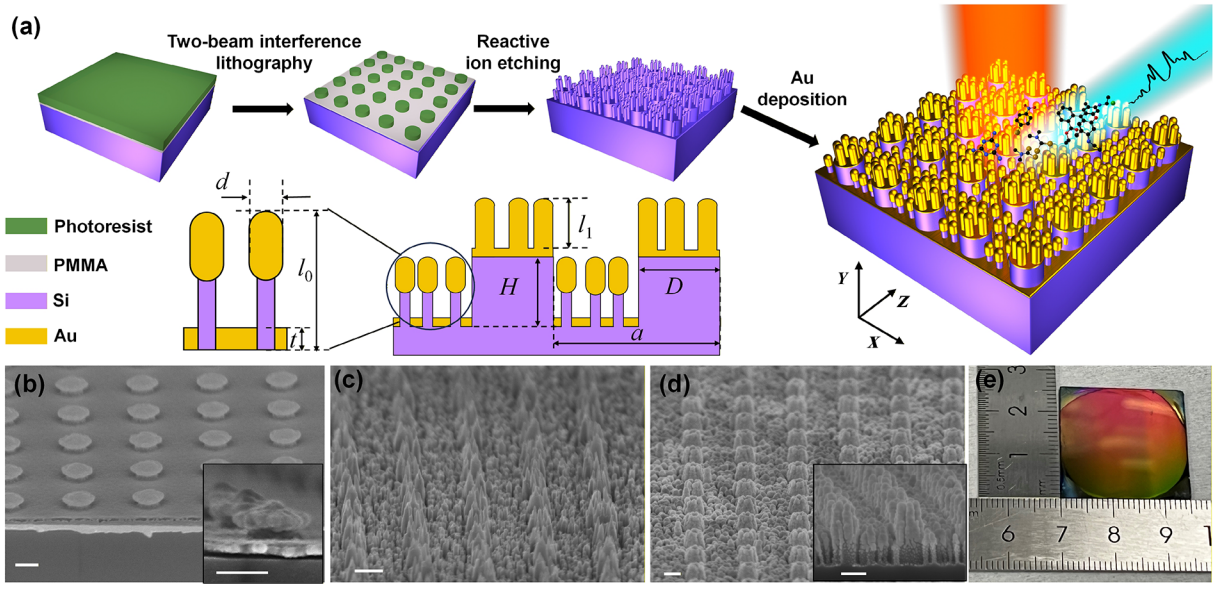

Figure 1 (a) Schematic illustration of the fabrication scheme of PNA-Si@Au NG. (b) Tilt-view SEM image of periodic mushroom-like photoresist arrays. (c) Tilt-view SEM image of periodic nanopillar arrays integrated with silicon nanograsses (named as PNA-Si NG). (d) Tilt-view SEM image of PNA-Si@Au NG. The scale bar is 200 nm. (e) Optical photograph over a larger area.

presented in Fig. 1(d). More details are provided in Experimental. Si nanograsses at both the top of the PNA and the non-PNA regions (i.e., the bottom of the PNA) are coated with an Au layer to form Si@Au nanograsses. Still, their morphologies differ significantly due to variations in the nanogap size between adjacent Si nanograsses. As shown in the SEM insets of Fig. 1(d) and Fig. S4(b) in the ESM, the Si@Au nanograsses at the PNA base exhibit a baseball bat-like shape, with thicker upper sections and narrower bottoms. This is because the Si nanograsses in this region have sub-20 nm gaps and heights > 100 nm (Fig. S4(a) in the ESM). During initial Au sputtering, a thin gold film with a thickness of ~ 10 nm was formed underneath due to limited Au atom deposition. Progressive coating thickening at the upper regions further blocks atomic ingress into gaps, resulting in the baseball bat shape. In contrast, the Si nanograsses at the PNA top have much larger gaps (Fig. S4(a) in the ESM), allowing Au atoms to migrate freely along the entire surface during sputtering and resulting in a uniform, continuous Au coating that fully encapsulates the Si nanograsses (Fig. 1(d) and Fig. S4(b) in the ESM). Additionally, the sample optical photograph in Fig. 1(e) shows relatively uniform structural diffraction light over an area of ~ 5 cm^2.

Nanoscale interparticle gaps are crucial for SERS enhancement. The average inter-nanograss gap distance of Si@Au nanograsses was controlled by tuning the RIE etching time and subsequent Au deposition via magnetron sputtering. RIE etching directly modulates the areal density of Si nanograsses. Based on the hypothesis that the distribution of Si@Au nanograsses is uniform, the average gaps width (s_x and s_z) in the x- and z-directions are identical and calculated by

$$s_x = s_z = \frac{1000}{\sqrt{n_{\mathrm{Si\,NG}}}} - \left(\frac{4A_{\mathrm{proj}}}{\pi n_{\mathrm{Si\,NG}}}\right)^{\frac{1}{2}} \quad (1)$$

where $n_{\mathrm{Si\,NG}}$ represents the areal density of Si nanograsses (i.e. the number of Si nanograsses per 1 μm^2); $A_{\mathrm{proj}}/n_{\mathrm{Si\,NG}}$ is the average projected area of Si@Au nanograsses on the x–z plane, statistically determined from SEM images (Figs. S5 and S6 in the ESM) using ImageJ software. The mechanism for controlling the areal density $n_{\mathrm{Si\,NG}}$ of Si nanograsses stems from the lateral etching effect induced by surface charge accumulation on the micro-mask during etching. This electric field-driven lateral ion etching creates trenches and fractures at the Si nanograss bases, reducing $n_{\mathrm{Si\,NG}}$ from 899 μm^{-2} (1 min) to 176 μm^{-2} (6 min), as shown in Table S1 in the ESM. As shown in Fig. S5(a) in the ESM, a continuous Au film without nanogaps formed after 1 min etching. After 2–3 min etching, nanoscale cracks and gullies emerged in the Au film, although the structure primarily consisted of clustered Si@Au nanograss aggregates (Figs. S5(b) and S5(c) in the ESM). At 4–6 min etching ($n_{\mathrm{Si\,NG}}$ is from 352 to 176 μm^{-2}), individual separated Si@Au nanograsses appeared (Figs. S5(d)–S5(f) in the ESM), with the average gap width ($s_x = s_z$) increasing from 4.8 ± 3.6 to 28.4 ± 9.8 nm. Furthermore, as shown in Fig. S6 and Table S2 in the ESM, the calculated average gap width between adjacent individual Si@Au nanograsses remains sub-10 nm (at approximately 5 nm) for different periodicities of PNA at the etching time of 4 min.

2.2 Optical properties of PNA-Si@Au NG

The core of the optimization strategy for SERS substrates requires spectral alignment of the excitation wavelength (633 nm) with the optical response characteristics of PNA-Si@Au NG to achieve maximum electromagnetic enhancement. It is revealed that controlling the areal density of Si nanograsses and the PNA period enables flexible tuning of periodic array-related plasmonic modes in PNA-Si@Au NG. As shown in Figs. 2(a) and 2(b), PNA-Si@Au NG exhibits two absorption peaks: a broad P1 peak at ~ 480 nm and a period-dependent P2 peak. Figure 2(c) shows that at a fixed period of 500 nm, increasing the areal density of Si nanograsses induces a slight redshift in the P2 peak, attributed to reduced interparticle gaps between adjacent Si@Au nanograsses. Overall, the inter-particle gap exhibits limited modulation on the P2 peak position. However, at a fixed gap of ~ 5 nm, increasing the PNA period from 400 to 700 nm induces a redshift of the P2 peak wavelength from 495 to 756 nm (Fig. 2(c)). When the PNA period is 600 nm and the gap is ~ 5 nm, the P2 peak reaches 644 nm, which matches the

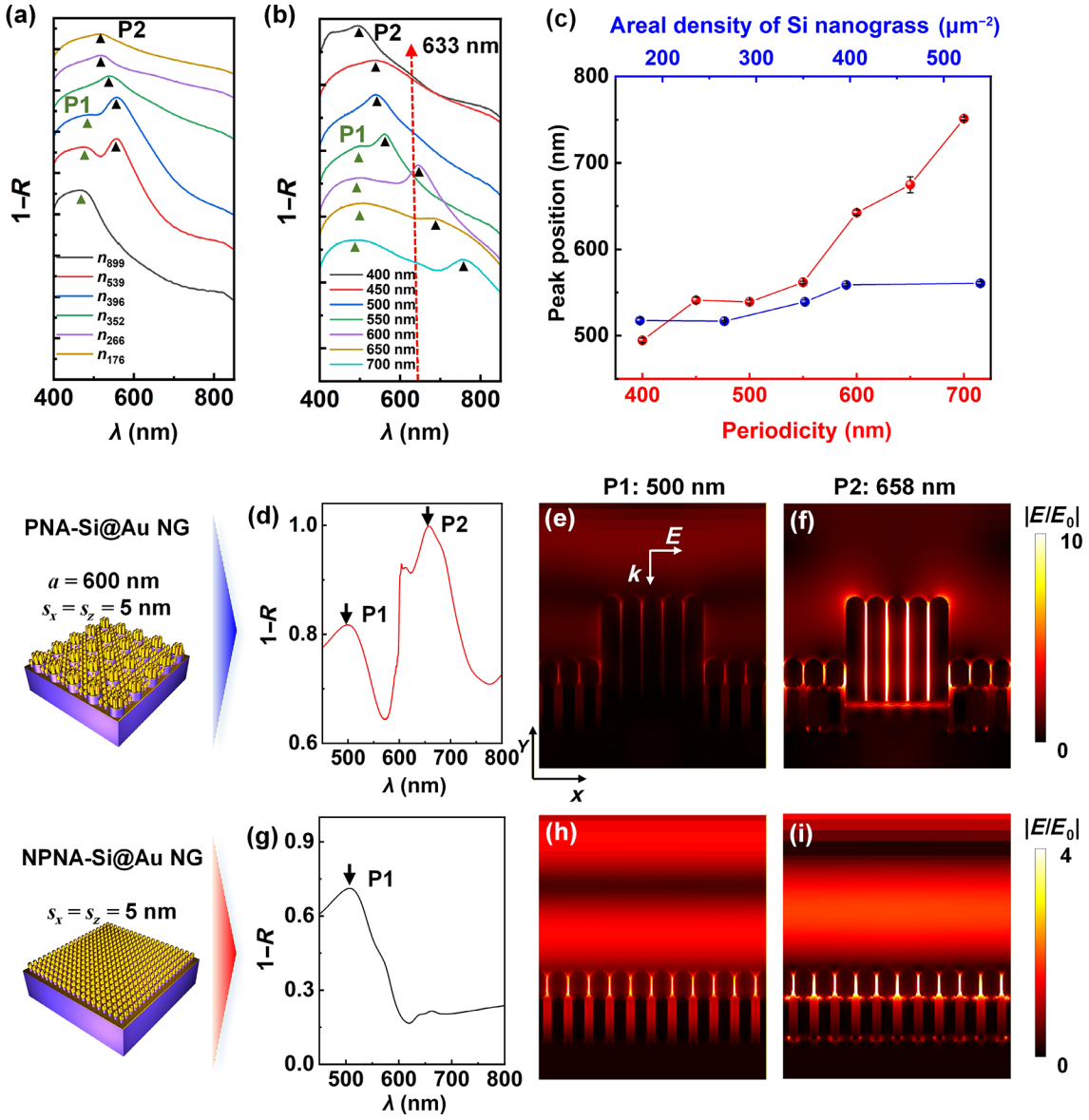

Figure 2 (a) Measured absorption spectra of PNA-Si@Au NG with a = 500 nm as a function of Si nanograss areal density; (b) measured absorption spectra of PNA-Si@Au NG as a function of period with a fixed Si nanograss areal density of ~ 352 μm^{-2} (gap ≈ 5 nm); (c) wavelength and intensity of the P2 resonance peak as a function of areal density and period. FDTD numerical simulated absorption spectra of (d) PNA-Si@Au NG and (g) NPNA-Si@Au NG; the electric field distribution and intensity of ((e) and (f)) PNA-Si@Au NG and ((h) and (i)) NPNA-Si@Au NG at the wavelength of 500 and 658 nm on the x–y planes. a = 600 nm, $s_x = s_z$ = 5 nm, D = 270 nm, H = 70 nm, d = 50 nm, l_0 = 190 nm, l_1 = 275 nm, t = 10 nm

experimental excitation wavelength (633 nm). These observations confirm that the absorption peaks in PNA-Si@Au NG originate from in-plane diffraction modes of the periodic array. By tuning the PNA period, spectral alignment between the excitation wavelength and the structure's optical response is achieved, which maximizes electromagnetic enhancement in the SERS substrate.

To analyze the optical properties of the PNA-Si@Au NG, we calculated the absorption spectra and corresponding electric field intensity distributions using the finite-difference time-domain (FDTD) method. The penetration depth d_p of light in silicon is given by

$$d_p = \lambda/4\pi k \quad (2)$$

where λ is the light wavelength in vacuum, and k is the extinction coefficient of silicon. Based on the extinction coefficient k from the Palik database [19], the penetration depth in silicon ranges from 80 to 9 μm across the wavelengths of 400–800 nm (k between 0.387 and 0.007). This is over 50 times smaller than the 525 μm-thick Si substrate. The transmitted light intensity decays to near-zero before reaching the substrate bottom. Moreover, the rough backsides of single-side-polished Si substrates suppress optical interference. The absorption spectrum is dominated by the nanostructure's reflectance properties with transmittance effectively negligible. Absorption is defined as $A = 1 - R$ in this work, and we obtained the absorption spectra through simulation or measurement of the corresponding reflection spectra. Here, to explore the role of the PNA acting on the optical properties of the PNA-Si@Au NG, we simplified the structure by replacing the randomly but vertically arranged Si@Au nanograss array (Fig. S7(a) in the ESM) with a regular one along the x- and z-directions (Fig. S7(b) in the ESM). It

is worth noting that we statistically analyzed the average values of the structural geometric parameters in the SEM images using ImageJ software, and these values were adopted as the core geometric features for the FDTD simulation. In addition, it was found that the average height of the Si@Au nanograsses at the PNA top was greater than that at the bottom, $l_1 > l_0$, which is due to the higher Si etching rate related to a large gap between Si@Au nanograsses at the PNA top (Figs. S7(c) and S7(d) in the ESM). The advantage of this modeling approach lies in eliminating random geometric noise to clarify the physical mechanism underlying the role of PNA, while reducing computational complexity to enable efficient and convergent calculations. This simplification is based on the fact that the separations between the nanorods (~ 5 nm) are much smaller than the wavelength of light used in the experiments, so only average values of Si@Au nanograss assembly parameters are important, and the deviations of the separations between the nanorods only have limited influence on the overall optical properties of an assembly of Si@Au nanograss [20, 21].

Figures 2(d)–2(i) present a side-by-side comparison of the absorption spectra and electric field distributions of PNA-Si@Au NG and NPNA-Si@Au NG (non-periodic nanopillar arrays integrated gold-capped silicon nanograsses) structures with identical sizes, shapes, and gaps. Figures 2(d) and 2(g) show the absorption spectra under a normal incident plane wave with the direction of electric field $\boldsymbol{E}$ aligned parallel to the lattice of the PNA. Both structures exhibit a peak around 500 nm (i.e., the P1 peak). As shown in Figs. 2(e) and 2(h), at the P1 peak, the electric field localizes at the gaps between Si@Au nanograsses. Furthermore, Fig. S8 in the ESM displays the localized electric field distributions of NPNA-Si@Au NG structure under the excitation field components ($\boldsymbol{E}_x$ and $\boldsymbol{E}_y$) at the P1 peak. The results indicate that the P1 peak corresponds to a transverse resonance mode, primarily driven by LSPR from the individual Si@Au nanograss through the electric field component $\boldsymbol{E}_x$ perpendicular to the long-axis of nanorods [11, 22]. Interestingly, instead of a flat curve with low absorption for the NPNA-Si@Au NG, there is another unexpected peak (marked by P2) appears in the periodic structure. Strong electric fields emerge at the gaps between Si@Au nanograsses both at the top and bottom of the PNA (Figs. 2(f) and 2(i)), indicating that the absorption peak results from an in-plane diffraction in air driven by the PNA (i.e., Wood's anomaly, WA) and the LSPR from the individual Si@Au nanograss [11, 23], which represent a lattice-period-dependent coupling mode.

The localized electric field enhancement strongly depends on the interparticle gaps, increasing significantly when gaps decrease below 10 nm [24–26]. To elucidate the role of the gap size, the absorption spectra, the electric field distribution and the intensity were simulated for PNA-Si@Au NG with a gap of 25 nm ($s_x = s_z$ = 25 nm). As shown in Fig. S9 in the ESM, PNA-Si@Au NG with a 25 nm gap also exhibits two absorption peaks, P1 (503 nm) and P2 (662 nm), corresponding to the LSPR from the individual Si@Au nanograss and the coupling mode between WA and the LSPR, respectively. In addition, at a gap of 25 nm, the interaction of the electric field between adjacent Si@Au nanograsses weakens significantly, resulting in a substantially lower intensity of the localized electric field compared to the gap of 5 nm.

2.3 SERS measurement of PNA-Si@Au NG

To demonstrate the PNA-based modulation on SERS performance, Rhodamine 6G (R6G), a commonly studied probe molecule for SERS sensing [27], was adsorbed on the samples involved in Figs. 2(a) and 2(b). To adsorb the target analytes, the surfaces of the substrates were immersed in R6G ethanol solution (10^{-6} M) for 1 h, then washed with ethanol solution and finally dried with flowing nitrogen. SERS sensitivity measurements were performed using a homemade Raman detection system with an iHR550 spectrometer (Horiba). The excitation laser with a wavelength of 633 nm was used. The laser power and signal acquisition time were 1.3 mW and 10 s, respectively (details can be found in the Experimental section). We also measured the SERS spectra under 532 nm excitation, and it was found that, compared to NPNA-Si@Au NG, there was no obvious signal amplification effect or reduction in the limit of detection (LOD) in PNA-Si@Au NG due to the absence of strong coupling between LSPR and Wood's anomaly near this wavelength (Fig. S10 in the ESM). SERS intensity was measured across varying areal densities of Si nanograss (directly governing Si@Au nanogaps) and PNA lattice periods, identifying the optimal structural parameters for SERS performance, as shown in Figs. 3(a) and 3(b). The SERS spectrum of R6G shows characteristic peaks at 1571 cm^{-1} corresponding to the C–O–C bond stretching vibration of R6G, while the peaks at 1313, 1359, 1512, and 1648 cm^{-1} correspond to the C–C stretching mode of R6G [27, 28]. As shown in Fig. 3(a), compared to the NPNA-Si@Au NG and pure gold film, the PNA-Si@Au NG presents a remarkable enhancement in Raman intensity. Figures 3(a) and 3(c) illustrate the measured SERS spectra taken from the R6G-modified PNA-Si@Au NG, all with a = 500 nm, but with the varying areal density of Si nanograss. The strongest Raman signal is obtained at the areal density of 352 μm^{-2}, corresponding to the average gap of ~ 5 nm. This phenomenon occurs because a high areal density results in a continuous Au film or Si@Au nanograss clusters after Au deposition, preventing the formation of dense but isolated Si@Au nanograsses. In contrast, a ~ 5 nm gap forms at 352 μm^{-2}, which generates strong hotspots and significantly enhancing SERS intensity. Further density reduction increases the gap, weakening the LSPR effect. Subsequently, with a fixed ~ 5 nm gap, the SERS spectra taken from the R6G-modified PNA-Si@Au NG with various PNA periodicities from 400 to 700 nm were studied. As shown in Figs. 3(b) and 3(c), the peak intensity at 1359 cm^{-1} first increases, then decreases with the increasing period. The highest Raman enhancement occurs at the periodicity of 600 nm. It is because the wavelength of the P2 mode (644 nm, a period-dependent resonant mode) in the sample with a = 600 nm is closer to the excitation wavelength (633 nm) than the ones with other periodicities.

For practical purposes, a reproducible signal is critical for SERS-related applications. To demonstrate the reproducibility of loading a periodic nanopillar array, we performed the SERS intensity measurement of 10^{-6} M R6G at 64 random points on a 10 mm × 10 mm sample area for the PNA-Si@Au NG (a = 600 nm, $s_x = s_z$ = 5 nm, D = 270 nm, H = 70 nm, d = 50 nm, l_0 = 190 nm, l_1 = 275 nm, t = 10 nm) and NPNA-Si@Au NG. As shown in Fig. 3(d), the NPNA-Si@Au NG exhibits an RSD of 28.5%, indicating significant signal intensity fluctuations, which arise from the non-uniform distribution of hotspots within the Si@Au nanograss aggregates and relative positional variations between analyte molecules and hotspots. In contrast, the PNA-Si@Au NG structure shows significantly improved signal consistency with the RSD of 11.6% (Fig. 3(e)), supporting the standard requirement for commercial SERS substrates (RSD < 20%). The traditional SERS-active substrates, such as random nanoparticle aggregates on a flat

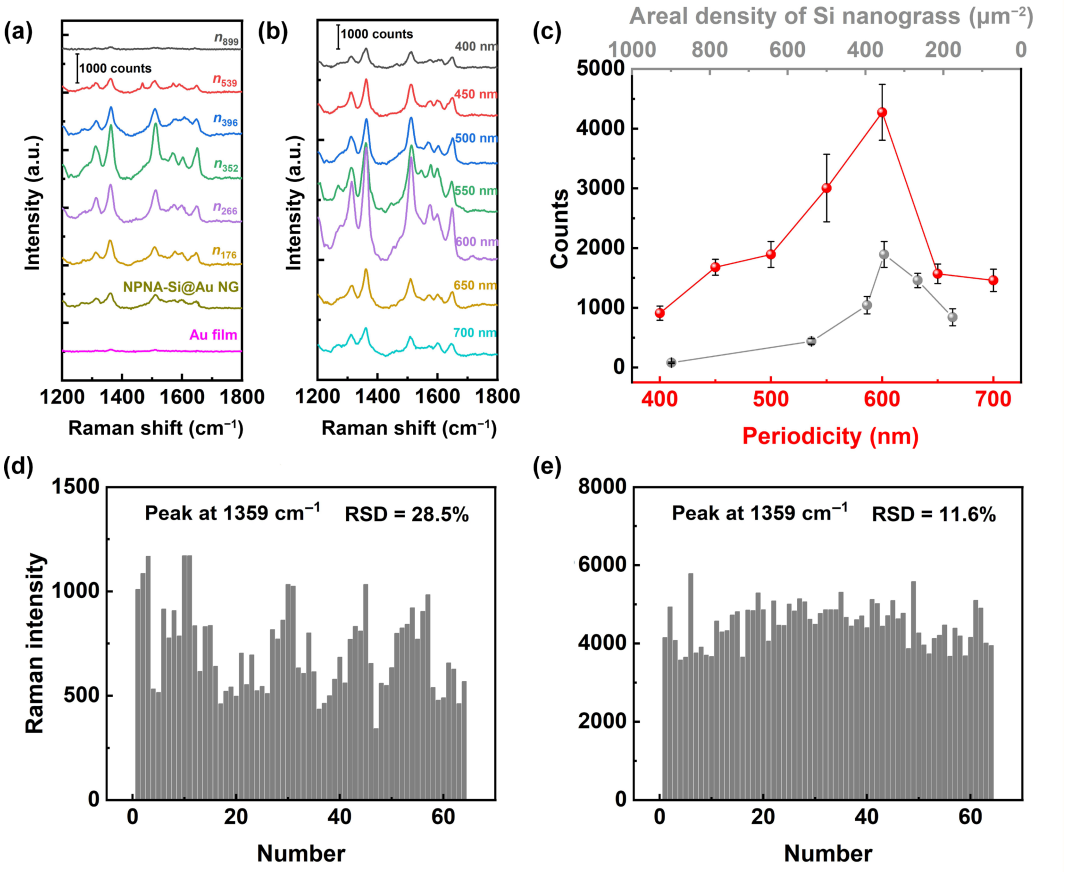

Figure 3 R6G detection. SERS spectra of 10^{-6} M R6G with different (a) areal densities of Si nanograss and (b) periods of PNA on the PNA-Si@Au NG substrate; (c) variation of the peak intensity at 1359 cm^{-1} as a function of Si nanograss areal density and PNA period. Reproducibility test on (d) NPNA-Si@Au NG and (e) PNA-Si@Au NG at 1359 cm^{-1} under the concentration of 10^{-6} M.

dielectric substrate (~ 30%) [29], the porous metamaterial structure (~ 20%) [30] and commercial Klarite substrate (~ 45%) [30], have high hotspot density but poor uniformity and fixed optical coupling modes. Compared to other uniform SERS substrates without nanoparticle assemblies, such as periodic gratings [31] or nanorod arrays [32], have RSD < 15% but low hotspot density leads to limited SERS enhancement capabilities. The reproducibility improvement of the PNA-Si@Au NG structure arises primarily from the synergistic coupling between the long-range periodicity of the PNA and the local Si@Au nanograsses. The periodic electromagnetic field distribution of the PNA (Wood's anomaly mode) integrates the LSPR of the nanograsses, forming a regularly distributed "macroscopic hotspot grid" across the substrate. Although randomly arranged Si@Au nanograsses generate dense but spatially uneven local hotspots, the periodic constraint of the PNA homogenizes these hotspots at the macroscopic level, significantly reducing spatial fluctuations in the SERS signal. In contrast, the NPNA-Si@Au NG structure lacks such periodicity, leading to larger variations in hotspot intensity and a correspondingly higher RSD (Figs. 3(d) and 3(e)). In a word, the introduction of PNA means that hotspots originate from strong coupling between the Si@Au nanograss assemblies and the periodic nanostructure, rather than from randomly distributed individual nanorods, effectively eliminating the effect of random fluctuations in the morphology and arrangement of the nanoparticle assemblies [11].

2.4 Potential application of PNA-Si@Au NG in SERS

To further demonstrate the versatility and sensitivity of the PNA-Si@Au NG (a = 600 nm, $s_x = s_z$ = 5 nm, D = 270 nm, H = 70 nm, d = 50 nm, l_0 = 190 nm, l_1 = 275 nm, t = 10 nm), 4-NBT, thiram and melamine were also used. 4-NBT ($C_6H_5NO_2S$) is an aromatic molecule with a thiol group. The H atom on the –SH group is readily replaced by Au, forming Au–S bond [33]. Figure 4(a) depicts the SERS spectra of a sample treated by a series of diluted 4-NBT ethanol solutions with varying concentrations. Vibrational peaks of 4-NBT appear at 1335 cm^{-1} (N–O vibration [33, 34]) and 1572 cm^{-1} (ring C–C stretching [35, 36]). Raman signal intensity at 1335 cm^{-1} decreases with reduced 4-NBT concentration. As shown in Fig. S11(a) in the ESM, the experimental data were fitted to an exponential function, resulting in R^2 = 0.96 at 1335 cm^{-1}. At the concentration of 10^{-8} M, the single intensity is very weak but still observable. The detection limit of PNA-Si@Au NG for 4-NBT is approximately 10 nM.

Thiram ($C_6H_{12}N_2S_4$), a broad-spectrum agricultural fungicide, is extensively applied for soil disinfection, seed treatment and disease control in fruits and vegetables [37]. Its use for foliar applications was banned by the European Union in 2019 due to proven oncogenic risks [5]. Notably, driven by economic interests, illegal thiram use persists. Establishing sensitive and accurate detection methods for thiram is crucial for ensuring the safety of agricultural products and protecting public health. Figure 4(b) depicts the SERS spectra of solid thiram powder and the PNA-Si@Au NG treated by

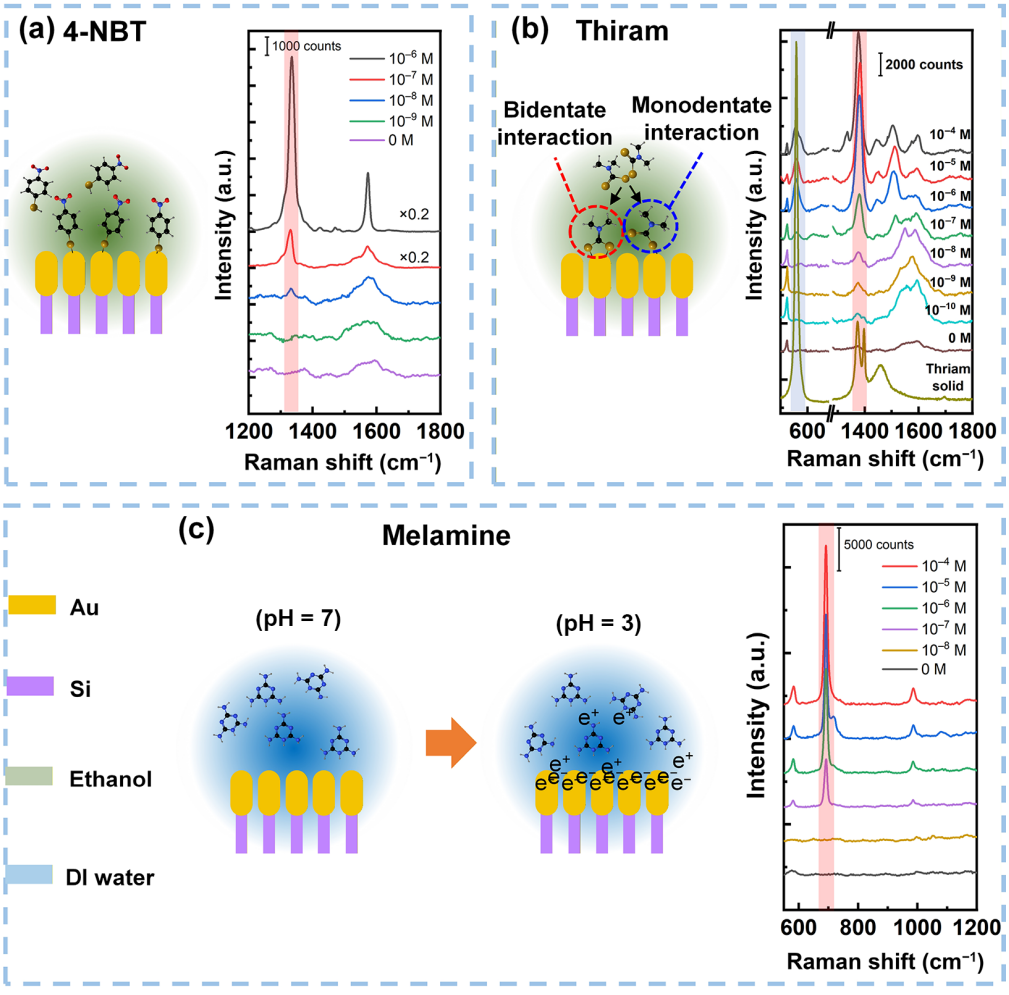

Figure 4 Adsorption mechanism and concentration-dependent SERS spectra recorded for different molecules adsorbed on the PNA-Si@Au NG. (a) 4-NBT, (b) thriam and (c) melamine under different concentrations. The size of PNA-Si@Au NG: a = 600 nm, $s_x = s_z$ = 5 nm, D = 270 nm, H = 70 nm, d = 50 nm, l_0 = 190 nm, l_1 = 275 nm, t = 10 nm

a series of diluted thiram ethanol solutions with varying concentrations. It can be seen that the Raman characteristic peaks of thiram molecules adsorbed on PNA-Si@Au NG differ significantly from the solid powder: The 558 cm^{-1} peak (S–S bond and C–S–S bond stretching vibration [5, 37]) intensity weakens, whereas the 1380 cm^{-1} peak (CH_3 bending vibration [5]) enhances. Thiram molecules undergo S–S bond cleavage on the gold surface, generating thiourea species [5], which enables the efficient adsorption of residual groups via Au–S bonds. As illustrated in Fig. 4(b), Au acts as an electrophile that binds to the two central S atoms (electron donors) of thiram, leading to S–S bond cleavage and the generation of two dimethyl residues. These residues can adsorb onto the Au surface via monodentate coordination (one S atom per residue) or bidentate coordination (two S atoms per residue) [38], consequently attenuating the 558 cm^{-1} peak intensity. While, the 1380 cm^{-1} peak intensity decreases with lower thiram concentration. As shown in Fig. S11(b) in the ESM, the experimental data were fitted to an exponential function, resulting in R^2 = 0.98 at 1380 cm^{-1}. The detection limit of PNA-Si@Au NG for thiram is approximately 1 nM, significantly improved compared to traditional detection approaches (liquid chromatography) and other SERS-active substrates based on Au nanoparticles (Table S3 in the ESM).

Melamine ($C_3H_6N_6$), an industrial compound with a nitrogen content of 66.7%, has been illicitly added to food to inflate protein detection values artificially. However, it exhibits high nephrotoxicity that may lead to renal failure and death [39]. Currently, China sets a limit of 1 mg/L (8×10^{-6} M) for melamine in infant formula and 2.5 mg/L (2×10^{-5} M) in other foods. Boisen et al. discovered that melamine molecules cannot effectively adsorb onto Au surfaces in neutral solutions, resulting in poor SERS performance of Au-coated nanostructured substrates [6]. However, melamine molecules undergo protonation in solution when pH < 5, acquiring positive charges [6]. Based on this, the PNA-Si@Au NG substrate was subjected to oxygen plasma etching before molecular adsorption. On the one hand, oxygen-etched substrates exhibit significantly increased wettability, enhancing the contact area between molecules and nanostructures. On the other hand, it generates abundant hydroxyl groups (–OH) on the substrate surface after oxygen etching, rendering it negatively charged in solution. This facilitates electrostatic adsorption with positively charged melamine molecules, as illustrated in Fig. 4(c). Figure 4(c) depicts the SERS spectra of a sample treated by a series of diluted melamine acid solutions (pH = 3) with varying concentrations. A characteristic peak appears at 691 cm^{-1}, attributed to the in-plane deformation vibration mode of the triazine ring in melamine [40]. Raman signal intensity at 691 cm^{-1} decreases with reduced melamine

concentration. As shown in Fig. S11(c) in the ESM, the relationship between SERS intensity and concentration is linear, with R^2 = 0.98 at 691 cm^{-1}. Notably, the drop coating-air drying method may cause uneven molecular adsorption and coffee ring formation, resulting in relatively large fluctuations in SERS signals and thus larger error bars. The detection limit of PNA-Si@Au NG for melamine is approximately 100 nM, significantly improved compared to traditional substrates based on single Au/Ag nanoclusters [41, 42]. In addition, as shown in Table S3 in the ESM, the PNA-Si@Au NG substrate exhibits a lower LOD than other detection approaches, such as liquid chromatography and mid- and near-infrared spectroscopy. Notably, this detection limit is lower than the thresholds required by food safety standards of China, indicating the potential of the PNA-Si@Au NG substrate for screening illegal additives in food products.

3 Conclusions

In summary, based on the concept of enhancing SERS performance through controllable hotspot construction on structured substrates, we proposed a strategy involving the introduction of a two-dimensional periodic nanopillar array into metal nanoparticle aggregates to regulate hotspot spatial arrangement and electromagnetic field coupling modes. Adjacent Si@Au nanograss gaps of approximately 5 nm were achieved via RIE etching and subsequent Au deposition via magnetron sputtering. At the same time, dual-beam interference lithography was used to control the structural period to match the excitation wavelength with the structure's optical response. The study revealed the coupling mechanism between lattice diffraction and localized surface plasmon resonance in Si@Au nanograss assemblies. High SERS signal reproducibility with RSD = 11.6% was achieved by tuning resonant modes through periodic array parameters, which minimizes random morphological variations, and reducing molecular positional sensitivity via high-density hotspot distribution. The substrate demonstrated detection limits of 10 nM for 4-NBT, 1 nM for thiram, and 100 nM for melamine. These results elucidate the interaction mechanisms between distinct molecular species and the SERS substrate, further demonstrating the development of a versatile substrate with broad applicability. These advantages indicate that our approach facilitates reliable, sensitive, and low-cost SERS detection technology, promising broad applications in analytical chemistry, environmental monitoring, food safety, and biomedicine.

4 Experimental

4.1 Chemicals

Polymethyl methacrylate (PMMA, M_W: 350,000) was purchased from Sigma-Aldrich. The positive photoresist (AR-P 3740) and the diluent (AR 300-12) were purchased from Allresist. Rhodamine 6G (R6G, 95%) and melamine (99%) were purchased from Sigma-Aldrich. 4-NBT (95%) and thiram (≥ 97%) were purchased from Aldrich.

4.2 Fabrication of PNA-Si@Au NG

First, a silicon wafer (thickness 525 ± 10 μm, orientation (100), single-side polished) was cleaved into 2.5 cm × 2.5 cm Si substrates. Before use, the substrates were cleaned by sequential ultrasonication in acetone, ethanol, and deionized (DI) water for 20 min each, dried with nitrogen gas, and baked on a hotplate at 120 °C to remove moisture. To enhance the adhesion between the photoresist and the Si substrate, a layer of PMMA film was spin-coated onto the substrate surface. A 1.25 wt.% PMMA/chlorobenzene solution (molecular weight: 350,000) was prepared. Using a spin coater, a PMMA/chlorobenzene film was spin-coated onto the Si substrate at 3000 rpm for 33 s. The substrate was then placed on a hotplate at 180 °C for 5 min to remove the chlorobenzene solvent, forming a PMMA film approximately 45 nm thick. Subsequently, a layer of photoresist film (AR-P 3740 photoresist diluted with AR 300-12 diluent at a mass ratio of 1:2.5) was spin-coated onto the PMMA film surface at 5000 rpm for 33 s. The substrate was baked on a hotplate at 95 °C for 90 s to remove solvent and enhance adhesion to the PMMA. The Si substrate coated with photoresist was placed on the sample stage of a dual-beam interference lithography system (Fig. S2 in the ESM). The shutter was opened for 22 s to complete one exposure. The substrate plane was then rotated by 90°, followed by a second 22 s exposure. The exposed substrate was immersed in developer solution (0.5 wt.% NaOH aqueous solution) for 11 s and then rinsed in DI water for 20 s.

Next, the exposed substrate was placed in a reactive ion etching (RIE, PlasmaPro System 100RIE, Wavetest) system for etching. The etching chamber pressure was set to 8 mTorr, power to 50 W, and etching time varied between 1 and 6 min. Etching was performed using an SF_6/O_2 gas mixture. After RIE etching, the sample was cleaned in acetone for 20 min to remove residual photoresist mask and PMMA.

Finally, the etched sample was placed on the sample stage of a magnetron sputtering system (VTC300, Shenyang Maikenuo Co., Ltd.). A layer of Au was deposited onto the surface of the PNA-Si NG structure. The argon (Ar) gas flow rate was set to 45 sccm, current to 35 mA, and the sputtering time to 150 s. During sputtering, the voltage was approximately 360 V, and the chamber pressure was approximately 1.7 Pa.

4.3 Numerical simulations

The simulations were performed using FDTD to generate the absorption spectra and electric field distributions. Bloch boundary conditions were applied in both *x*- and *z*-axes. A mesh size of 2 nm for the metal region was utilized. The dielectric permittivity of gold was taken from Johnson and Christy, and that of Si was taken from the Palik. The PNA-Si@Au NG structure was excited by a plane wave incident normally along the *y*-axis, with the electric field polarized along the *x*-axis. A mesh size of 2 nm for the metal region was utilized. The FDTD model is shown in Fig. S5 in the ESM. Model parameters were set based on the average values of experimentally fabricated PNA-Si@Au NG structures, with structural parameters defined as follows: a = 600 nm, $s_x = s_z$ = 5 nm, D = 270 nm, H = 70 nm, d = 50 nm, l_0 = 190 nm, l_1 = 275 nm, t = 10 nm.

4.4 Characterizations

The surface morphologies of all the samples were characterized with scanning electron microscopy (AURIGA, Zeiss) working at 3–5 kV. All samples' reflection and transmission spectra were carried out using a UV–visible spectrophotometry (Lambda 950, PerkinElmer).

4.5 SERS measurements

Different molecular adsorption methods and testing conditions were employed for different target molecules. The prepared SERS substrates were cut into multiple samples. For R6G, samples with

varying Si nanograss densities (i.e., different gap sizes) and PNA periods were immersed in 10^{-6} M R6G ethanol solution for 1 h. After removal, the samples were rinsed extensively with ethanol to eliminate residual R6G and then dried under a nitrogen flow. For 4-NBT and thiram, samples were immersed in ethanol solutions of varying concentrations for 4 h, followed by extensive ethanol rinsing and nitrogen drying. For melamine, acidic aqueous solutions (pH = 3) at different concentrations were prepared. Substrates underwent 30 s oxygen plasma etching (TS-SY05, Tonson Tech Automation Equipment Co. Ltd., 120 W power, 20 mL/min oxygen flow rate) to enhance surface hydrophilicity and electronegativity. Subsequently, a 5 μL test solution was deposited on samples and air-dried. Within 60 min after etching, the contact angle of a 3 μL DI droplet remains as low as 20° (Fig. S12 in the ESM), confirming excellent hydrophilicity of the substrate before melamine molecule adsorption on the surface of PNA-Si@Au NG structure.

Raman measurements were performed using a homemade Raman detection system with a spectrometer (iHR550, Horiba). A 633 nm pump laser (08-NLD, Cobolt) was focused onto the sample surface. The reflected light (including Raman signals) was collected by an objective (100×, NA = 0.9) and a polarizer, ensuring that the incident electric field paralleled the PNA lattice vector to excite LSPR in Si@Au nanograss effectively. The laser power focused on the sample surface was 1.3 mW. Signal acquisition times were set to 10 s for R6G/4-NBT and 30 s for thiram/melamine. The SERS sensitivity test was measured at 5 random points on each sample. And the SERS uniformity test was measured at 64 random points on each sample.

Electronic Supplementary Material: Supplementary material (detailed methodology, statistics of structural parameter data, additional SEM image, and additional FDTD simulation analysis) is available in the online version of this article at https://doi.org/10.26599/NR.2026.94908563.

Data availability

All data needed to support the conclusions in the paper are presented in the manuscript and the Electronic Supplementary Material. Additional data related to this paper may be requested from the corresponding author upon request.

Acknowledgements

This work is granted by the National Natural Science Foundation of China (Nos. 12374414, 11974438, and 91850106).

Declaration of competing interest

All the contributing authors report no conflict of interests in this work.

Author contribution statement

N. Z.: Data curation, experimental design, validation, writing manuscript. Y. L.: Experimental design, validation. X. Y. S.: Project administration. Y. S.: Project administration, data curation. X. L. T.: Project administration, validation. C. J. J.: Project administration, experimental design, funding acquisition, writing manuscript.

Use of AI statement

None.

References

[1] Kim, G. H.; Son, J.; Nam, J. M. Advances, challenges, and opportunities in plasmonic nanogap-enhanced Raman scattering with nanoparticles. *ACS Nano* **2025**, *19*, 2992–3007.

[2] Lian, S.; Li, X. Q.; Lv, X. F. Recent developments in SERS microfluidic chips: From fundamentals to biosensing applications. *ACS Appl. Mater. Interfaces* **2025**, *17*, 10193–10230.

[3] Chin, L. K.; Yang, J. Y.; Chousterman, B.; Jung, S.; Kim, D. G.; Kim, D. H.; Lee, S.; Castro, C. M.; Weissleder, R.; Park, S. G. et al. Dual-enhanced plasmonic biosensing for point-of-care sepsis detection. *ACS Nano* **2023**, *17*, 3610–3619.

[4] Zhang, W. Q.; Yang, L. Y.; Song, Y.; Xu, H. Y. Gold nanostars: From synthesis, properties to their application in food hazard detection. *Chem. Eng. J.* **2025**, *506*, 160257.

[5] Anh, N. H.; Doan, M. Q.; Dinh, N. X.; Huy, T. Q.; Tri, D. Q.; Le, A. T. Gold nanoparticles-based SERS nanosensor for thiram and chloramphenicol monitoring in food samples: Insight into effects of analyte molecular structure on their sensing performance and signal enhancement. *Appl. Surf. Sci.* **2022**, *584*, 152555.

[6] Viehrig, M.; Rajendran, S. T.; Sanger, K.; Schmidt, M. S.; Alstrøm, T. S.; Rindzevicius, T.; Zór, K.; Boisen, A. Quantitative SERS assay on a single chip enabled by electrochemically assisted regeneration: A method for detection of melamine in milk. *Anal. Chem.* **2020**, *92*, 4317–4325.

[7] Fleischmann, M.; Hendra, P. J.; McQuillan, A. J. Raman spectra of pyridine adsorbed at a silver electrode. *Chem. Phys. Lett.* **1974**, *26*, 163–166.

[8] Stiles, P. L.; Dieringer, J. A.; Shah, N. C.; Van Duyne, R. R. Surface-enhanced Raman spectroscopy. *Annu. Rev. Anal. Chem.* **2008**, *1*, 601–626.

[9] Li, J. F.; Huang, Y. F.; Ding, Y.; Yang, Z. L.; Li, S. B.; Zhou, X. S.; Fan, F. R.; Zhang, W.; Zhou, Z. Y.; Wu, D. Y. et al. Shell-isolated nanoparticle-enhanced Raman spectroscopy. *Nature* **2010**, *464*, 392–395.

[10] Chirumamilla, M.; Toma, A.; Gopalakrishnan, A.; Das, G.; Zaccaria, R. P.; Krahne, R.; Rondanina, E.; Leoncini, M.; Liberale, C.; De Angelis, F. et al. 3D nanostar dimers with a sub-10-nm gap for single-/few-molecule surface-enhanced Raman scattering. *Adv. Mater.* **2014**, *26*, 2353–2358.

[11] Shen, Y.; Cheng, X. Z.; Li, G. Z.; Zhu, Q. Z.; Chi, Z. G.; Wang, J. F.; Jin, C. J. Highly sensitive and uniform surface-enhanced Raman spectroscopy from grating-integrated plasmonic nanograss. *Nanoscale Horiz.* **2016**, *1*, 290–297.

[12] Zhang, N.; Liang, D. Y.; Shen, Y.; She, X. Y.; Jin, C. J. Grating-integrated gold nanograsses encapsulated with ZIF-8: A quantitative and ultrasensitive surface-enhanced Raman scattering substrate. *ACS Appl. Mater. Interfaces* **2024**, *16*, 39917–39926.

[13] Wang, H. H.; Liu, C. Y.; Wu, S. B.; Liu, N. W.; Peng, C. Y.; Chan, T. H.; Hsu, C. F.; Wang, J. K.; Wang, Y. L. Highly Raman-enhancing substrates based on silver nanoparticle arrays with tunable sub-10 nm gaps. *Adv. Mater.* **2006**, *18*, 491–495.

[14] Lee, W.; Lee, S. Y.; Briber, R. M.; Rabin, O. Self-assembled SERS substrates with tunable surface plasmon resonances. *Adv. Funct. Mater.* **2011**, *21*, 3424–3429.

[15] Bauman, S. J.; Darweesh, A. A.; Furr, M.; Magee, M.; Argyropoulos, C.; Herzog, J. B. Tunable SERS enhancement via sub-nanometer gap metasurfaces. *ACS Appl. Mater. Interfaces* **2022**, *14*, 15541–15548.

[16] Sweedan, A. O.; Pavan, M. J.; Schatz, E.; Maaß, H.; Tsega, A.; Tzin, V.; Höflich, K.; Mörk, P.; Feichtner, T.; Bashouti, M. Y. Evolutionary optimized, monocrystalline gold double wire gratings as a novel SERS sensing platform. *Small* **2024**, *20*, 2311937.

[17] Natan, M. J. Concluding remarks: Surface enhanced Raman scattering. *Faraday Discuss.* **2006**, *132*, 321–328.
[18] Azziz, A.; Safar, W.; Xiang, Y.; Edely, M.; de la Chapelle, M. L. Sensing performances of commercial SERS substrates. *J. Mol. Struct.* **2022**, *1248*, 131519.
[19] Palik, E. D. *Handbook of Optical Constants of Solids*; Academic Press: London, 1985.
[20] Kabashin, A. V.; Evans, P.; Pastkovsky, S.; Hendren, W.; Wurtz, G. A.; Atkinson, R.; Pollard, R.; Podolskiy, V. A.; Zayats, A. V. Plasmonic nanorod metamaterials for biosensing. *Nat. Mater.* **2009**, *8*, 867–871.
[21] Wurtz, G. A.; Dickson, W.; O'Connor, D.; Atkinson, R.; Hendren, W.; Evans, P.; Pollard, R.; Zayats, A. V. Guided plasmonic modes in nanorod assemblies: Strong electromagnetic coupling regime. *Opt. Express* **2008**, *16*, 7460–7470.
[22] Fang, Y.; Seong, N. H.; Dlott, D. D. Measurement of the distribution of site enhancements in surface-enhanced Raman scattering. *Science* **2008**, *321*, 388–392.
[23] Shen, Y.; Zhou, J. H.; Liu, T. R.; Tao, Y. T.; Jiang, R. B.; Liu, M. X.; Xiao, G. H.; Zhu, J. H.; Zhou, Z. K.; Wang, X. H. et al. Plasmonic gold mushroom arrays with refractive index sensing figures of merit approaching the theoretical limit. *Nat. Commun.* **2013**, *4*, 2381.
[24] Chen, X. S.; Park, H. R.; Pelton, M.; Piao, X. J.; Lindquist, N. C.; Im, H.;Kim, Y. J.; Ahn, J. S.; Ahn, K. J.; Park, N. et al. Atomic layer lithography of wafer-scale nanogap arrays for extreme confinement of electromagnetic waves. *Nat. Commun.* **2013**, *4*, 2361.
[25] Park, H. R.; Chen, X. S.; Nguyen, N. C.; Peraire, J.; Oh, S. H. Nanogap-enhanced terahertz sensing of 1 nm thick ($\lambda/10^6$) dielectric films. *ACS Photonics* **2015**, *2*, 417–424.
[26] Zhang, C.; Lia, C. H.; Yu, J.; Jiang, S. Z.; Xu, S. C.; Yang, C.; Liu, Y. J.; Gao, X. G.; Liu, A. H.; Man, B. Y. SERS activated platform with three-dimensional hot spots and tunable nanometer gap. *Sens. Actuat. B Chem.* **2018**, *258*, 163–171.
[27] Wang, L.; Li, C. H.; Cao, C. F.; Lei, F. C.; Zhao, X. F.; Li, Z.; Zhang, C.; Jiao, Y.; Yu, J. Multifunctional polymeric nanoneedles with "full-spectrum intrinsic internal standard" for precise SERS biosensing. *Adv. Funct. Mater.* **2025**, *35*, 2416789.
[28] Huang, C. L.; Zhao, H. H.; Peng, Z. X.; Zheng, B.; Zhang, C.; Wang, J. One-step fabrication of highly dense gold nanoparticles on polyamide for surface-enhanced Raman scattering. *Appl. Surf. Sci.* **2021**, *561*, 149856.
[29] Wang, X.; Li, M. H.; Meng, L. Y.; Lin, K. Q.; Feng, J. M.; Huang, T. X.; Yang, Z. L.; Ren, B. Probing the location of hot spots by surface-enhanced Raman spectroscopy: Toward uniform substrates. *ACS Nano* **2014**, *8*, 528–536.
[30] Zhang, X. Y.; Zheng, Y. H.; Liu, X.; Lu, W.; Dai, J. Y.; Lei, D. Y.; MacFarlane, D. R. Hierarchical porous plasmonic metamaterials for reproducible ultrasensitive surface-enhanced Raman spectroscopy. *Adv. Mater.* **2015**, *27*, 1090–1096.
[31] Liu, Y.; Tian, X. R.; Guo, W. R.; Wang, W. Q.; Guan, Z. Q.; Xu, H. X. Real-time Raman detection by the cavity mode enhanced Raman scattering. *Nano Res.* **2019**, *12*, 1643–1649.
[32] Zhu, Z. D.; Shi, X. Y.; Feng, Y. T.; He, M.; Ye, C.; Zhou, H. Y.; Zhang, M. F.; Zhang, W.; Li, J. H.; Jiang, C. L. Lotus leaf mastoid inspired Ag micro/nanoarrays on PDMS film as flexible SERS sensor for *in-situ* analysis of pesticide residues on nonplanar surfaces. *Spectrochim. Acta A Mol. Biomol. Spectrosc* **2023**, *288*, 122211.
[33] Jia, D. C.; Cheng, R.; McNeely, J. H.; Zong, H. H.; Teng, X. Y.; Xu, X. X.; Cheng, J. X. Ultrasensitive infrared spectroscopy via vibrational modulation of plasmonic scattering from a nanocavity. *Sci. Adv.* **2024**, *10*, eadn8255.
[34] Wang, M. Y.; Yan, Y. Z.; Zhao, C.; Jiang, Y. J. Laser parallel nanofabrication of dual-Au-nanoholes on microsphere-lens-array for polarization-dependent SERS. *Adv. Mater. Technol.* **2024**, *9*, 2302244.
[35] Lartey, J. A.; Harms, J. P.; Frimpong, R.; Mulligan, C. C.; Driskell, J. D.; Kim, J. H. Sandwiching analytes with structurally diverse plasmonic nanoparticles on paper substrates for surface enhanced Raman spectroscopy. *RSC Adv.* **2019**, *9*, 32535–32543.
[36] Ding, Q. Q.; Wang, J.; Chen, X. Y.; Liu, H.; Li, Q. J.; Wang, Y. L.; Yang, S. K. Quantitative and sensitive SERS platform with analyte enrichment and filtration function. *Nano Lett.* **2020**, *20*, 7304–7312.
[37] Chen, M.; Luo, W.; Liu, Q.; Hao, N. Y.; Zhu, Y. Q.; Liu, M. Z.; Wang, L. M.; Yang, H.; Chen, X. Q. Simultaneous *in situ* extraction and fabrication of surface-enhanced Raman scattering substrate for reliable detection of thiram residue. *Anal. Chem.* **2018**, *90*, 13647–13654.
[38] Sánchez-Cortés, S.; Domingo, C.; García-Ramos, J. V.; Aznárez, J. A. Surface-enhanced vibrational study (SEIR and SERS) of dithiocarbamate pesticides on gold films. *Langmuir* **2001**, *17*, 1157–1162.
[39] Wu, Y. N.; Zhang, Y. Analytical chemistry, toxicology, epidemiology and health impact assessment of melamine in infant formula: Recent progress and developments. *Food Chem. Toxicol.* **2013**, *56*, 325–335.
[40] Guo, Z. N.; Cheng, Z. Y.; Li, R.; Chen, L.; Lv, H. M.; Zhao, B.; Choo, J. One-step detection of melamine in milk by hollow gold chip based on surface-enhanced Raman scattering. *Talanta* **2014**, *122*, 80–84.
[41] Kaleem, A.; Azmat, M.; Sharma, A.; Shen, G. X.; Ding, X. T. Melamine detection in liquid milk based on selective porous polymer monolith mediated with gold nanospheres by using surface enhanced Raman scattering. *Food Chem.* **2019**, *277*, 624–631.
[42] Zhang, X. L.; Xiao, X. H.; Dai, Z. G.; Wu, W.; Zhang, X. G.; Fu, L.; Jiang, C. Z. Ultrasensitive SERS performance in 3D "sunflower-like" nanoarrays decorated with Ag nanoparticles. *Nanoscale* **2017**, *9*, 3114–3120.